Materials Research. 2021; 24(2): e20200377
DOI: https://doi.org/10.1590/1980-5373-MR-2020-0377

Synthesis of TiO_2 Tubes Via Dissolution of $TiOSO_4$ Rod Using H_2O_2

*Maykon A. Montanhera[a], Ricardo H. D. Venancio[b], Éder Alves Pereira[a], Renato G. Freitas[b], Fernando R. de Paula[a]**

[a]*Universidade Estadual Paulista, Faculdade de Engenharia, Ilha Solteira, SP, Brasil*
[b]*Universidade Federal de Mato Grosso, Departamento de Química, Laboratório Computacional de Materiais (LCM), Cuiabá, MT, Brasil*

Received: August 18, 2020; Revised: December 26, 2020; Accepted: January 25, 2021

We demonstrate here for the first time an original and facile approach to preparing titanium oxide (TiO_2) tubes using hydrogen peroxide (H_2O_2) and titanyl (IV) oxysulfate ($TiOSO_4$) as sacrificial templates. The method involves dissolving $TiOSO_4$ powder in H_2O_2 solution and subsequently applying thermal treatment on the resulting amorphous precipitate. Prepared samples were characterized by X-ray diffraction, scanning electron microscopy (SEM) images, thermogravimetric (TG) analysis, and UV-vis analysis. Experimental results indicated that the samples exhibit tube-like structures with lengths of approximately 1.9 μm in diameter and 11.5 μm in length. Anatase and rutile phases were formed after annealing at different temperatures in air. The crystallite size estimated by Rietveld refinement showed an increase from 34.69 to 354.28 nm with an increase in the annealing temperature from 600 to 1000 °C. At the same time, the band gap values decreased from 3.14 to 2.97 eV. The electron density maps were calculated, and the electronic density was observed to increase from 497.56 $e^- Å^{-2}$ (600 °C) to 533.10$e^- Å^{-2}$ (740 °C) and decrease with the annealing temperature of samples. A possible mechanism for the formation of TiO_2 tubes was proposed.

Keywords: *TiO_2 tubes, titanyl sulfate, template-free, sacrificial template.*

1. Introduction

After the discovery by Fujishima and Honda that TiO_2 could be used as an electrode to split water into hydrogen[1], its photocatalysis began to attract much more attention. The photocatalysis of TiO_2 is of great interest owing to its chemical stability, non-toxic characteristics, low cost, UV light absorption, photo-corrosion resistance, and oxidative properties.

TiO_2 exists mainly in three different crystalline habits: rutile (tetragonal), anatase (tetragonal), and brookite (orthorhombic). The photocatalytic performance of anatase is considered superior when compared to the other phases; this is attributed to a higher density of localized states and slower charge carrier recombination[2,3]. The anatase phase possesses a considerable bandgap energy of 3.2 eV; thus, it can only be excited under UV light irradiation. When excitation occurs, electrons from the valence band jump to the conduction band, leaving behind positive holes (h^+). The electrons and holes diffuse to the particle surface of the TiO_2. When the holes react with water, free-radical oxidation can occur, which is capable of degrading organic dyes.

It is a well-known fact that the factors that affect the photocatalytic properties of TiO_2 include crystallinity, microstructure, surface area, phase composition, light harvesting, separation rate of photogenerated charges, and energy band structure. Hence, morphological control is a strategy to be considered for improving TiO_2 photocatalytic performance[4].

TiO_2 nanoparticles are widely applied in water and wastewater treatment because of their stronger catalytic activity. This increase in catalytic activity has been attributed to their smaller size, which has permitted a larger surface area per unit mass.

However, TiO_2 nanoparticles also have disadvantages, with the most important and critical being toxicity[5-7]. A large number of published studies have revealed that TiO_2 nanoparticles could be translocated through the pulmonary route to the brain or the systemic circulation through which other organs such as the kidney or liver could be reached.

Presently, TiO_2 tubes have attracted considerable interest because of their improved photocatalysis performance and lower toxicity than nanoparticles. TiO_2 tubes have many useful features, such as a high surface-to-volume ratio and multi-channel structure, making them convenient for mass transfer. The high surface area allows adsorbing many chemicals, and the unique structure makes better use of light through multiple reflections within its space[8].

In this present study, we report an original and facile synthetic approach to the preparation of anatase TiO_2 tubes, using rod-like $TiOSO_4$ powder as a sacrificial template in the presence of H_2O_2. Different from most methods that use high-temperature processes, expensive precursors, or preparation instruments, our approach is eco-friendly and

*e-mail: depaula@dfq.feis.unesp.br

does not require expensive precursor reagents, exhibits reduced reaction time, and is template-free.

2. Experimental Procedure

2.1. Experimental section

2.1.1. Preparation TiO_2 tubes

In the preparation of the titanium precursor, 0.002 mol L^{-1} of titanyl (IV) oxysulfate ($TiOSO_4$) rods, purchased from Sigma Aldrich, was dissolved in 2000 mL distilled water at 26 °C under magnetic stirring, and then, 0.392 mol L^{-1} of hydrogen peroxide (H_2O_2/35 wt. in H_2O . Sigma Aldrich) was added to the solution. A yellow-colored acidic solution with a yellow precipitate was formed, indicating the formation of peroxo complex of titanium solution ($TiO(OH)_2$)[9]. The $TiO(OH)_2$ precipitate obtained was washed for 3–4 times with water by vacuum filtration until most of the impurity SO_4^{2-} was removed and then dried at 60 °C. Finally, the precipitate was annealed in air at different temperatures ranging from 600 to 1000 °C for 4 h to obtain crystalline TiO_2 tubes. The following chemical reaction scheme (Equations 1-3) is suggested during the formation of TiO_2 tubes:

$$TiOSO_4 + H_2O_2 \rightarrow Ti(O_2)SO_4 + H_2O \quad (1)$$

$$Ti(O_2)SO_4 + 2OH^- + (x+1)H_2O \rightarrow TiO(OH)_2 \cdot xH_2O + H_2O_2 + SO_4^{2-} \quad (2)$$

$$TiO(OH)_2 \xrightarrow{\Delta} TiO_2 + H_2O \quad (3)$$

2.1.2. Materials characterization

The structures of the as-prepared samples, as well as the heat-treated sample, were studied by XRD at room temperature (25 °C) with a SHIMADZU XRD-6000 model, which provides Cu *Kα* radiation (λ = 1.544 Å). Measurements were taken in θ–2θ configurations from 20° to 65°, with a step size of 0.2° min^{-1}. To obtain the microstructural data of the TiO_2 tubes, a Rietveld refinement[10] was performed using the General Structure Analysis System program[11] suite with the EXPGUI interface[12]. The original Rietveld formulation and many of its successors[13] consider the diffraction line width as a smooth function of the *d*-spacing of the diffraction angle (2θ, whereas many peaks of interest near 2θ have very different widths). Hence, in this study, the peak profile function developed by Stephens[14] was used to model the experimental data. In this method, considerations are made for diffraction widths that are not a smooth function of *d*, which might arise from anisotropic sample-size broadening or from a particular pattern of defects (e.g., stacking faults). Finally, the bi-dimensional model for the crystallite size described by Larson and Von Dreele[11] was used to account for the anisotropy in the half-width of the reflection.

The electron density maps were calculated following the method previously described in detail[15]. In brief, a point (x, y, z) of the crystallite cell with volume (V) was calculated by Fourier series using the structural factors F(h, k, l):

$$\rho(x,y,z) = V^{-1} \sum_h \sum_k \sum_l F(h,k,l) exp\left[2\pi i(hx,ky,lz)\right] \quad (4)$$

where (x, y, z) represents vector (r) of real space, with one vector space (a, b, c) and another vector (h, k, l), which represent the coordinates of one vector from the reciprocal space with base (a*, b*, c*), i.e., they are the coordinates from the diffraction plane, which is given by Bragg's Law. The electron density distribution in the plane {slice 1 with $x = y = z = 1$ (i.e., face *a b c*), with set (*h k l*) as the projection plane (101)} was calculated.

A UV–Vis spectrophotometer (Varian Cary 100) with an integrating sphere attachment DRA-CA-30I for diffuse reflectance measurements was used to establish the optical band gap. Optical absorption was measured in the 250–1000 nm range. SEM images were obtained with a ZEISS model EVO LS15 with an acceleration voltage of 0.1–20.0 kV coupled with an EDX analyzer for stoichiometry. TG was performed using the TA Instruments Q60 under a nitrogen atmosphere from 30 °C to 1000 °C at a heating rate of 3 °C/min.

3. Results and Discussion

3.1. Mechanism for the formation of TiO_2 tubes

The process of the morphology evolution to obtain TiO_2 tubes is summarized in Figure 1. The tubular structure is obtained via an in-situ reaction and the dissolution of $TiOSO_4$. In the process of synthesis, when the $TiOSO_4$ reacts with H_2O_2, a yellow-colored solution is immediately obtained, indicating the formation of peroxo complexes of titanium. This yellow-colored solution yields a water-insoluble yellow gel, titanium oxyhydroxide, that is maintained at room temperature. The formation of titanium oxyhydroxide occurs preferentially in the surface of the rod where the precursor has full contact with the reaction solution. As the reaction time increases, the $TiOSO_4$ in the central part of the rod that has not reacted with H_2O_2 begins to be dissolved by the water present in the solution, resulting in the formation of a void space. According to Tian et al.[16] the center part of the rod has considerable surface energy and shows a greater tendency to dissolve.

3.2. SEM images

The obtaining the crystalline TiO_2 tubes and the morphological evolution process of tube formation as a function of reaction time is showed in Figure 2. As seen in Figure 2a, the initial precursor, titanium oxysulfate, exhibits a rod structure of approximately 2.3 μm in diameter and 13.8 μm in length. After 6 h (2b) and 12 h (2c) reactions, those rods evolved, for the most part, into a tubular structure, presenting a lot of tiny particles on the surface. Increasing the reaction time to 24 h (2d) is observed only tubular structure with a uniform diameter of 1.9 μm and walls characterized by a smooth surface, with a reduction in the number of particles on the surface with average size 460 nm.

After the synthesis of the precursors, we investigated the effect of calcination on the precursors' morphology. After calcination at a temperature of 740 e 800 °C (Figures 2e, 2f)

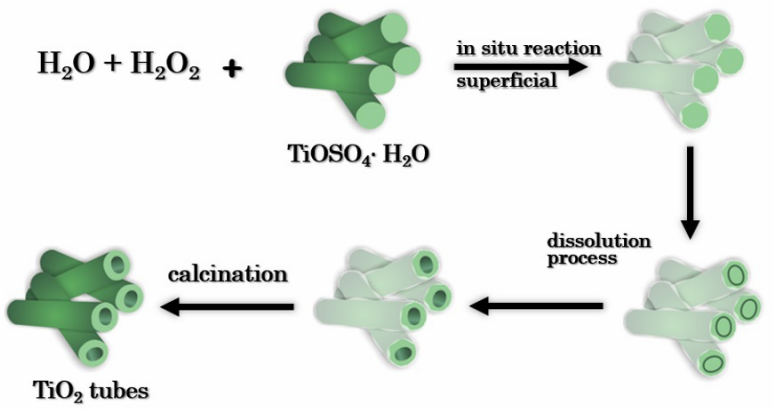

Figure 1. Schematic illustration of the formation process of the TiO_2 tubes.

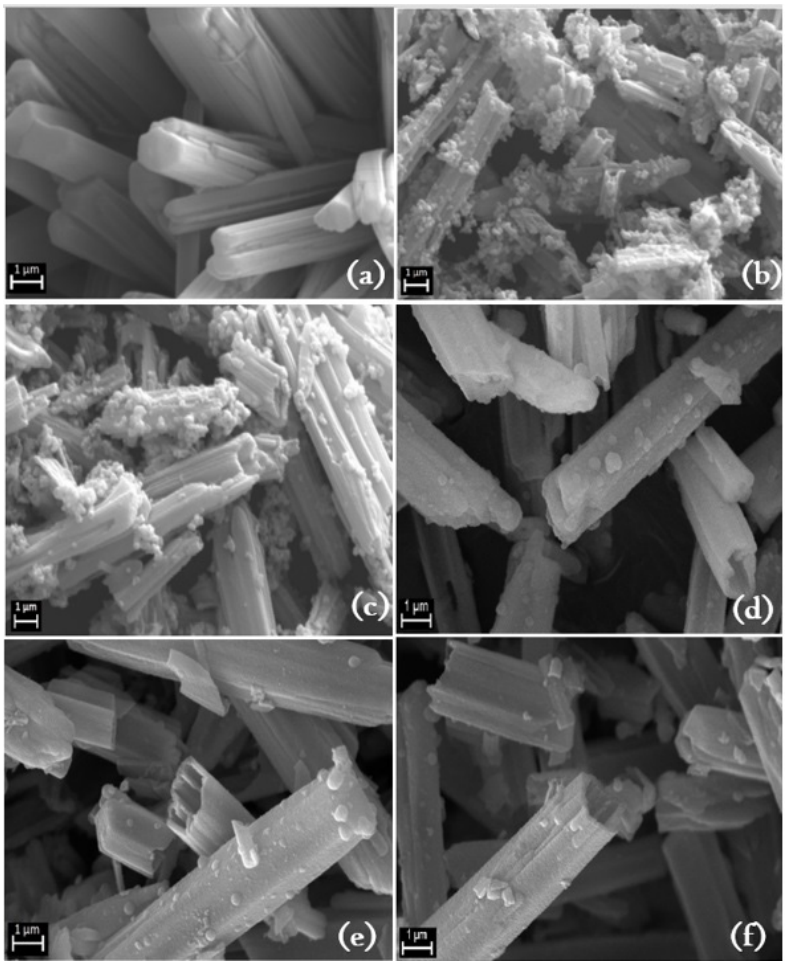

Figure 2. Scanning electronic micrograph (SEM) images of the titanyl (IV) oxysulfate ($TiOSO_4$) rods (a) and peroxo complexes of titanium (b-d). Images of the precursors annealed at different temperatures: (e) 740 and (f) 800 °C.

respectively, the hollow tube structure is maintained, suggesting the excellent thermal stability of the tubes.

3.3. TG analysis

The TG of the TiO_2 precursor after drying at 60 °C for 24 h is shown in Figure 3. The weight loss is 11.6% as the temperature increase from 20 to 155 ºC, with the loss of free water and bound moisture, as well as some surface hydroxide radicals. A mass loss of about 5% occurs in the temperature range of 155 to 390 °C; this is attributed to the thermal decomposition of the peroxo-titanium complex and is due to the removal of sulfur. In the range of 390 to 700 °C, the

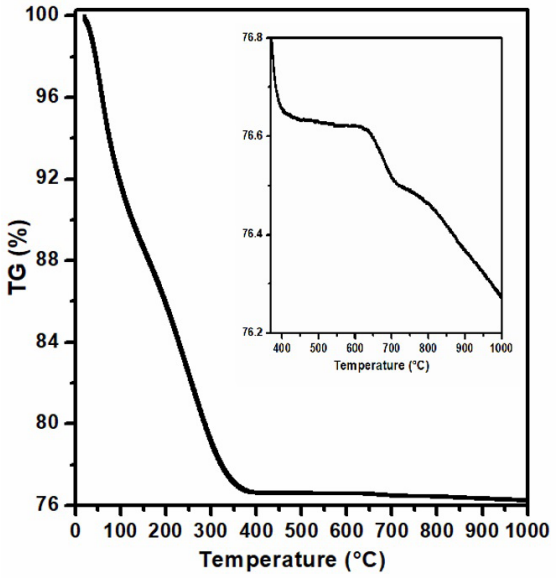

Figure 3. TG thermograms of the TiO_2 precursor.

phase conversion from amorphous to anatase occurs, and in the range of 700 to 1000 °C the phase conversion from anatase to rutile phase take places.

3.4. X-ray analysis

Techniques of structural refinement, such as XRD, are robust in revealing qualitative and quantitative information of phase composition and lattice parameters. In this sense, we used Rietveld[11,17] refinement for all TiO_2 tubes obtained in this study, with the data presented in the Supplementary Information (SI). As can be observed, Figure 4 displays the XRD patterns of the peroxo-titanium complex obtained and of the starting material $TiOSO_4$. There are differences between $TiOSO_4$ and the peroxo-titanium complex. The XRD pattern of $TiOSO_4$ (Figure 4a) shows two sharp peaks at about 10.7° and 18.8°; however, these peaks did not appear in the XRD patterns of the peroxo-titanium complex (as-prepared), indicating the occurrence of a chemical reaction and the formation of the amorphous titanium precursor. The XRD patterns of the samples annealed at 600, 700, 740, 800, and 1000 °C for 4 h are also shown in Figure 4b. The position of the peaks associated with anatase and rutile polymorphs was taken from ICDD 00-021-1272 and ICDD 01-076-0317, respectively. At a sample annealing temperature of 600 °C, the XRD pattern shows only the anatase phase; meanwhile, at 700 °C and 740 °C, the main content is the anatase phase with a modest amount of rutile, 6% and 12% respectively. With increasing annealing temperature, the presence of rutile phase increases; thus, for sample annealing at 800 °C, the amount of rutile is 50% and, finally for the samples at 1000 °C, only the rutile phase is present. The full-width at half-maximum (FWHM) of the 101 diffraction peak of pure-phase anatase decreased with increasing annealing temperature, suggesting that the average crystallite size increased through thermal treatment. In fact, the crystallite size estimated by Rietveld refinement, reported in Table 1 for the pure-phase anatase annealed at 600 °C was 34.69 nm, and for the pure-phase rutile obtained at 1000 °C, the average crystallite size was 354.28 nm.

By analyzing the Rietveld refinement obtained for all TiO_2 tubes, it is possible to obtain fundamental information regarding the electronic structure of such samples as Fourier electron density maps. These electronic density maps can be observed in Figure 5.

Several papers in the literature[18-22] have described physicochemical properties tuned with the Fourier electron density maps obtained by Rietveld refinement[10,11]. Many of those papers[23-27] also observed similar Fourier electron density maps obtained by Rietveld refinement[10,11] of TiO_2 with several types of morphology. Freitas et al.[22] observed an increase in dielectric relaxation[26], electronic lifetime[27], Debye length screening[27] and yield of water splittingfor $BaBi_4Ti_4O_{15}$ nanoparticles, CdSe@TiO_2 nanotubes, and TiO_2 nanotubes, respectively. In this study, we observed similar results, whereas it is possible to observe that the electronic density increases from 497.56 e^- Å^{-2} (600 °C) to 533.10 e^- Å^{-2} (740 °C). In addition, it is observed that by increasing the rutile phase amount, as observed in Table 1 for TiO_2 tubes obtained at 800 °C, the electronic density decreases to 513.90 e^- Å^{-2}, as observed in Figure 5. It is important to stress that all electronic density obtained herein for TiO_2 tubes were obtained along the anatase (101) plane.

The tunning of electronic and structural properties can be observed not only for nanotubes, but also for several other morphologies such as nanocube[28], nanocone[29], nanopillar[30], nanoplate[31], nanopyramid[32], nanorod[33,34], nanosheet[35], nanosphere[36,37] and nanowire[38,39]. He et al.[33] studied lead-free (K,Na)NbO_3 nanorods arrays and observed that both, the charge density map and deformation charge density map exhibit asymmetric charge distribution along the [110] orientation, which should be due to the displacement of Nb atom from the center position toward the [110] direction. Botelho et al.[37] studied structural and electronic properties of $CaMoO_4$ nanospheres using electron density maps. According to the authors[37], the color scale of each map represents zones of high and low electronic densities, i.e., the blue and red regions have a high electronic density and no electronic charge, respectively. Therefore, the authors[37] obtain in a fundamental point of view the position of electron and hole along the semiconductor. Nanowires morphology is also an important nano-morphology for several devices' studies. In this sense, Degtyarev et al.[39] studied the effect of geometry, doping and surface states in InAs nanowires. The authors observed that electron space distribution and the electron density in the intrinsic InAs nanowires are strongly affected by the charged surface states, nanowire width and doping. The dominating type of the electron space distribution is tubular with additional electron accumulation regions at the nanowire corners coupled to each other. Therefore, electron density map is pivotal for the fundamental comprehension and tuning of electronic and structural effects as consequence of a-priori morphology.

3.5. UV-vis analysis

The bandgaps of the synthesized TiO_2 tubes were investigated by UV–Vis diffuse reflectance spectra following the Kubelka–Munk (K–M) formula[40]:

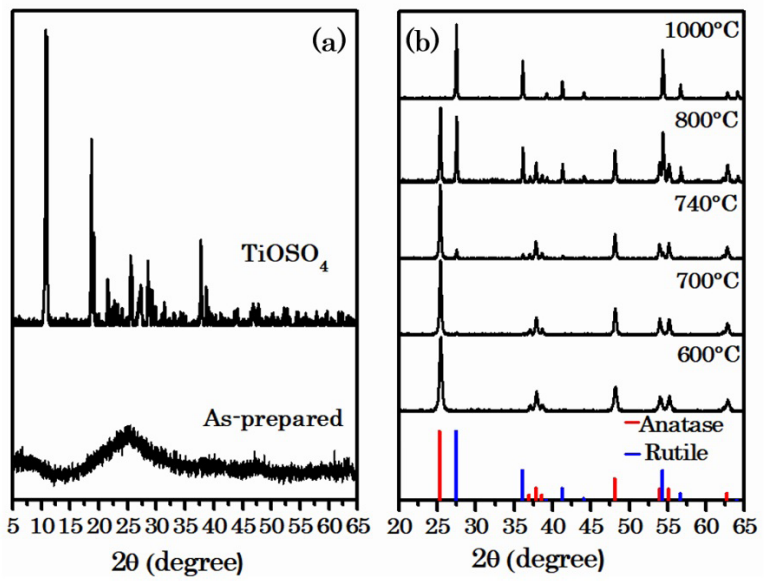

Figure 4. (a) XRD patterns of commercial rod-like $TiOSO_4$ and the precursors obtained before calcination. (b) Corresponding products after calcination at different temperatures.

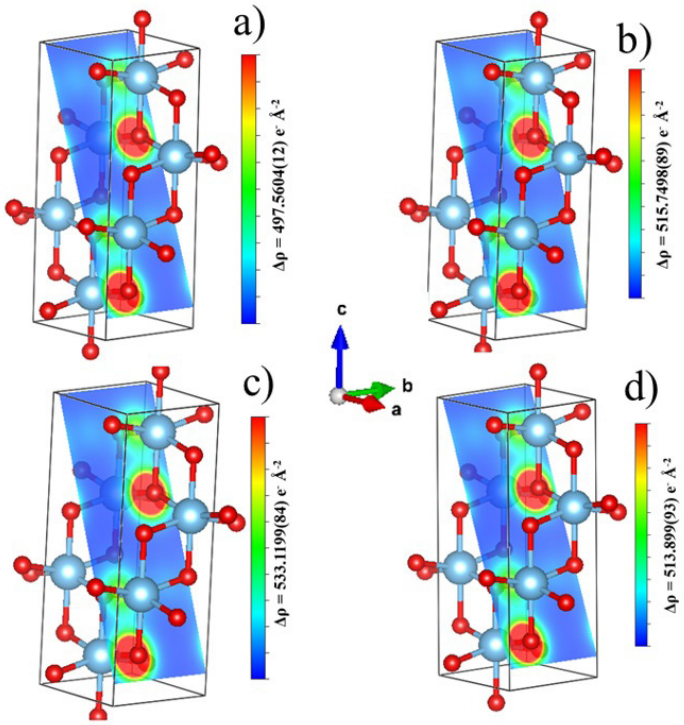

Figure 5. Electron density maps of Fourier obtained from Rietveld refinement for (101) anatase-TiO_2 tubes obtained at a) 600 °C, b) 700 °C, c) 740 °C and d) 800 °C.

$$F(R_\infty) = K/S = \left[(1-R_\infty)^2\right]/2R_\infty \quad (5)$$

where R_∞ is the absolute diffuse reflectance for an infinitely thick sample, and K and S are the sample absorption and scattering coefficients, respectively. The energy of the band gap is calculated by extrapolating a straight line to the abscissa axis. The plots of K/S versus E_g from UV–Vis spectrum data of the samples annealed at 600 °C, and 1000 °C were estimated to be 3.14 eV and 2.97 eV for the phase-pure anatase and rutile, respectively. When the calcination temperature increases, the band gap decreases. These values are consistent with those obtained by Landmann et al.[41]. All dates obtained are reported in Table 1.

Table 1. Crystallite size, phase content and gap energy of TiO_2-tubes calcined at different temperatures.

Calcination temperature (°C)	Amount of each phase (wt%)		Crystallite size (nm)		gap (eV)
	Anatase	Rutile	Anatase	Rutile	
600	100.00	-	34.69	-	3.14
700	94.11	5.88	66.57	33.27	3.10
740	87.98	12.01	96.26	129.24	3.00
800	49.64	50.35	198.42	210.14	2.98
1000	-	100.00	-	354.28	2.97

4. Conclusion

In this study, we described a novel method with a simple approach, efficient and low cost, for the preparation of large-diameter TiO_2 tubes via dissolution of rod-like $TiOSO_4$ using H_2O_2. Anatase and rutile phase was formed after annealing at different temperatures in air. TiO_2 tubes obtained after annealing exhibited a tubular structure with a uniform diameter of 1.9 μm and walls characterized by a smooth surface and small particles on the surface. XRD analysis showed that annealing at temperatures higher than 600 °C resulted in the evident transformation of the anatase phase into the rutile phase. Pure rutile phase was obtained by annealing nanostructured anatase at 1000 °C. The crystallite size estimated by Rietveld refinement increased from 34.69 to 354.28 nm with an increase in the annealing temperature from 600 to 1000 °C. At the same time, the band gap values decreased from 3.14 to 2.97 eV. Fourier electron density maps obtained by Rietveld refinement was possible to observe that the electronic density increases from 497.56 $e^- Å^{-2}$ (600 °C) to 533.10 $e^- Å^{-2}$ (740 °C) and for TiO_2 tubes obtained at 800 °C, the electronic density decreases to 513.90 $e^- Å^{-2}$.

In summary, this study provides a novel pathway to the synthesis of TiO_2 tubes with an eco-friendly approach that does not require an expensive precursor, exhibits reduced reaction time, and is template-free. This novel pathway offers a new material platform for catalysis, photovoltaic cell, and other applications.

5. Acknowledgements

The authors thank the Brazilian agencies: FAPESP (2018/14052-6)) and CNPq (427161/2016-9), for financial support.

6. References

1. Fujishima A, Honda K. Electrochemical photolysis of water at a semiconductor electrode. Nature. 1972;238(5358):37-8.
2. Carp O, Huisman CL, Reller A. Photoinduced reactivity of titanium dioxide. Prog Solid State Chem. 2004;32(1-2):33-177.
3. Ismagilov ZR, Tsikoza LT, Shikina NV, Zarytova VF, Zinoviev VV, Zagrebelnyi SN. Synthesis and stabilization of nano-sized titanium dioxide. Russ Chem Rev. 2009;78(9):873-85.
4. Es-Souni M, Es-Souni M, Habouti S, Pfeiffer N, Lahmar A, Dietze M, et al. Brookite formation in TiO_2Ag nanocomposites and visible-light-induced templated growth of ag nanostructures in TiO_2. Adv Funct Mater. 2010;20(3):377-85.
5. Oberdorster G, Ferin J, Lehnert BE. Correlation between particle size, in vivo particle persistence, and lung injury. Environ Health Perspect. 1994;102:173-9.
6. Zhao J, Bowman L, Zhang X, Vallyathan V, Young SH, Castranova V, et al. Titanium dioxide (TiO_2) nanoparticles induce JB6 cell apoptosis through activation of the caspase-8/Bid and mitochondrial pathways. Environ Health A. 2009;72(19):1141-9.
7. Lee KP, Trochimowicz HJ, Reinhardt CF. Pulmonary response of rats exposed to titanium dioxide (TiO_2) by inhalation for two years. Toxicol Appl Pharmacol. 1985;79(2):179-92.
8. Joo JB, Dahl M, Li N, Zaera F, Yin Y. Tailored synthesis of mesoporous TiO_2 hollow nanostructures for catalytic applications. Energy Environ Sci. 2013;6(7):2082-92.
9. Karuppuchamy S, Nonomura K, Yoshida T, Sugiura T, Minoura H. Cathodic electrodeposition of oxide semiconductor thin films and their application to dye-sensitized solar cell. Solid State Ion. 2002;151(1-4):19-27.
10. Rietveld HM. Profile refinement method for nuclear and magnetic structures. J Appl Cryst. 1969;2(2):65-71.
11. Larson AC, Von Dreele RB. General Structure Analysis System (GSAS). Los Alamos: Los Alamos National Laboratory Report (LAUR); 2004. (vol. 86).
12. Toby BH. *EXPGUI*, a graphical user interface for *GSAS*. J Appl Cryst. 2001;34(2):210-3.
13. Thompson P, Cox DE, Hastings JB. Rietveld refinement of Debye-Scherrer synchrotron X-ray data from Al2O3. J Appl Cryst. 1987;20(2):79-83.
14. Stephens PW. Phenomenological model of anisotropic peak broadening in powder diffraction. J Appl Cryst. 1999;32(2):281-9.
15. March NH. Electron density theory of atoms and molecules. New York: Academic Press; 1992. Chapter 1.
16. Tian G, Chen Y, Bao H-L, Meng X, Pan K, Zhou W, et al. Controlled synthesis of thorny anatase TiO_2 tubes for construction of Ag–AgBr/TiO2 composites as highly efficient simulated solar-light photocatalyst. J Mater Chem. 2012;22(5):2080-8.
17. Rietveld HM. A profile refinement method for nuclear and magnetic structures. J Appl Cryst. 1969;2(2):65-71.
18. Saravanakumar S, Sivaganesh D, Ali KSS, Robert MC, Rani MP, Chokkalingam R, et al. Analysis of structural, optical and charge density distribution studies on Zn1-xMnxS nanostructures. Physica B. Physics of Condensed Matter. 2018;545:134-40.
19. Itoh T, Imai H. Electrochemical cycling effect on structural parameters and electron density of $Li_{1-x}Ni_{0.5}Mn_{1.5}O_4$ using synchrotron X-ray analyses. Physica B. Physics of Condensed Matter. 2018;532:64-70.
20. Antoinette MM, Israel S, Sathya G, Amali AJ, Berchmans JL, Sujatha K, et al. Experimental charge density distribution and its correlation to structural and optical properties of Sm^{3+} doped Nd_2O_3 nanophosphors. J Rare Earths. 2017;35(11):1102-14.
21. Robert MC, Saravanan R. Triple phase structure and electron density analysis of the thermoelectric material $Bi_{80}Sb_{20}$. Powder Technol. 2010;197(3):159-64.
22. Freitas RG, Santanna MA, Pereira EC. Dependence of TiO_2 nanotube microstructural and electronic properties on water splitting. J Power Sources. 2014;251:178-86.
23. Murugesan S, Thirumurugesan R, Mohandas E, Parameswa P. X-ray diffraction Rietveld analysis and Bond Valence analysis

of nano titania containing oxygen vacancies synthesized via sol-gel route. Mater Chem Phys. 2019;225:320-30.
24. Ullah B, Sayyadi-Shahraki A, Ullah A, Khan R. Dielectric abnormality and high-permittivity microwave dielectric properties of SrO-TiO_2-CeO_2 solid solution. Ceram Int. 2019;45(3):3634-42.
25. Li J, Yang S, Liu J, Zhuang Y, Tian Y, Hu Q, et al. Colossal dielectric behavior of Co-doped TiO_2 ceramics: a comparative study. J Alloys Compd. 2019;786:377-84. http://dx.doi.org/10.1016/j.jallcom.2019.01.356.
26. Almeida PMV, Gozzo CB, Thaines EHNS, Sales AJM, Freitas RG, Terezo AJ, et al. Dielectric relaxation study of the ceramic matrix $BaBi_4Ti_4O_{15}$:Bi_2O_3. Mater Chem Phys. 2019;205:72-83.
27. Freitas RG, Lucas FWS, Santanna MA, Mendes RA, Terezo AJ, de Souza GLC, et al. An experimental and theoretical study on the electronic and structural properties of CdSe@ TiO2 nanotube arrays. Physical Chemistry. Phys Chem Chem Phys. 2016;18(38):26885-93.
28. Merk V, Nerz A, Fredrich S, Gernert U, Selve S. Optical properties of silver nanocube surfaces obtained by silane immobilization. Nanospectroscopy. 2014;1:19-25.
29. Mehrvar L, Sadeghipari M, Tavassoli SH, Mohajerzadeh S, Fathipour M. Optical and surface enhanced raman scattering properties of Ag modified silicon double nanocone array. Sci Rep. 2017;7(1):12106.
30. Yan W, Dottermusch S, Reitz C, Richards BS. Hexagonal arrays of round-head silicon nanopillars for surface anti-reflection applications. Appl Phys Lett. 2016;109(14):143901.
31. Keast VJ, Walhout CJ, Pedersen T, Shahcheraghi N, Cortie MB, Mitchell DRG. Higher order plasmonic modes excited in ag triangular nanoplates by an electron beam. Plasmonics. 2016;11:1081-6.
32. Vasconcelos TL, Archanjo BS, Oliveira BS, Valaski R, Cordeiro RC, Medeiros HG, et al. Plasmon-tunable tip pyramids: monopole nanoantennas for near-field scanning optical microscopy. Adv Opt Mater. 2018;6(20):1-6.
33. He Y, Wang Z, Hu X, Cai Y, Li L, Gao Y, et al. Orientation-dependent piezoresponse and high-performance energy harvesting of lead-free (K,Na) NbO_3 nanorod arrays. RSC Advances. 2017;28(28):16908-15.
34. Thupakula U, Jena A, Khan AH, Dalui A, Acharya S. Synthesis, structure and electronic properties of ultranarrow CdS nanorods. J Nanopart Res. 2012;14(1):1-11.
35. Fabris GSL, Marana NL, Laranjeira JAS, Longo E, Sambrano JR. New two-dimensional zinc oxide nanosheets: Properties, stability, and interconversion. Mater Lett. 2020;275:128067.
36. Gouveia AF, Vieira VEM, Sczancoski JC, Lemos PS, Rout SK, Arul NS, et al. Electronic structure, morphological aspects, and photocatalytic discoloration of three organic dyes with $MgWO_4$ by the complex polymerization method. J Inorg Organomet Polym Mater. 2020;30(8):2952-70.
37. Botelho G, Nogueira IC, Moraes E, Longo E. Study of structural and optical properties of $CaMoO_4$ nanoparticles synthesized by the microwave-assisted solvothermal method. Mater Chem Phys. 2016;183:110-20.
38. Diao Y, Liu L, Xia S, Feng S. Early stages of Cs adsorption mechanism for GaAs nanowire surface. Appl Surf Sci. 2018;434:950-6.
39. Degtyarev VE, Khazanova SV, Demarina NV. Features of electron gas in InAs nanowires imposed by interplay between nanowire geometry, doping and surface states. Sci Rep. 2017;7(1):3411.
40. Sirita J, Phanichphant S, Meunier FC. Quantitative analysis of adsorbate concentrations by diffuse reflectance FT-IR. Anal Chem. 2007;79(10):3912-8.
41. Landmann M, Rauls E, Schmidt WG. The electronic structure and optical response of rutile, anatase and brookite TiO_2. J Phys Condens Matter. 2012;24(19):195503-8.

Supplementary material

The following online material is available for this article:

Figure S1 - X-ray diffractograms-Rietveld refinement plot of TiO2 tubes at a) 600°C, b) 700°C, c) 740°C, d) 800°C and e) 1000°C.

Table S1 - Structural parameters obtain using Rietveld refinement for TiO2 tubes.